Nature Communications
https://doi.org/10.1038/s41467-026-76310-z

Article in Press

The recent enhancement of the surface melt over the Antarctic Peninsula dictated by thermodynamics

Received: 26 October 2025

Accepted: 23 July 2026

Published online: 04 August 2026

Cite this article as: Zhang, Q., Huai, B., Wang, S. *et al.* The recent enhancement of the surface melt over the Antarctic Peninsula dictated by thermodynamics. *Nat Commun* (2026). https://doi.org/10.1038/s41467-026-76310-z

Qinglin Zhang, Baojuan Huai, Sai Wang, Brice Noël, Michiel R. van den Broeke, Xavier Fettweis, Christoph Kittel, Dahe Qin & Minghu Ding

The recent enhancement of the surface melt over the Antarctic Peninsula dictated by thermodynamics

Qinglin Zhang[1,2], Baojuan Huai[3], Sai Wang[1], Brice Noël[4], Michiel R. van den Broeke[5], Xavier Fettweis[4], Christoph Kittel[4,6], Dahe Qin[1], Minghu Ding[1,2]*

1. State Key Laboratory of Disaster Weather Science and Technology, Chinese Academy of Meteorological Sciences, Beijing, China

2. Department of Atmospheric and Oceanic Sciences & Institute of Atmospheric Sciences & Key Laboratory of Polar Atmosphere-Ocean-Ice System for Weather and Climate, Ministry of Education, Fudan University, Shanghai

3. College of Geography and Environment, Shandong Normal University, Jinan, China

4. Laboratory of Climatology, Department of Geography, SPHERES research unit, University of Liège, Liège, Belgium

5. Institute for Marine and Atmospheric Research Utrecht, Utrecht University, Utrecht, Netherlands

6. Physical Geography Research Group, Department of Geography, Vrije Universiteit Brussel, Brussels, Belgium

Corresponding to: Minghu Ding (dingminghu@foxmail.com)

Abstract: Intense surface melt and subsequent meltwater ponding are the key triggers for the disintegration of ice shelves in the Antarctic Peninsula (AP). Although a long-term decline in AP surface melt has been evident since the early 1990s, episodes of intense surface melt events have frequently been reported in recent years. Here, using 1979-2023 daily surface melt rates from regional climate models, we show that this declining trend has reversed, with November–February surface melt increasing significantly by 3% year^{-1} (p < 0.05) between 2009 and 2022. Decomposition of trends based on circulation classification indicates that changes in the frequency of atmospheric circulation patterns cannot account for this enhancement. Instead, the thermodynamics—linked to variations in the surface energy budget independent of atmospheric circulation contribute 80% of the positive trend in AP surface melt. Analysis of extreme surface melt events further supports the dominant thermodynamic contribution.

Introduction

Surface melt plays a pivotal role in regulating the stability and mass balance of the glaciers in the Antarctic Peninsula (AP), particularly for the flat ice shelves which are sensitive to meltwater ponding[1-3]. In addition to ocean-waves impacts and basal melt[4,5], intensive meltwater production potentially triggers ice shelf disintegration through hydrofracturing[2,6-8], one mode of mass loss of the AP ice shelves[8,9]. Historical records reveal that most AP ice shelf hydrofracturing events were preceded by anomalously high surface melt[7-9]. Quantifying AP surface melt volume/rate is therefore critical for understanding the formation of melt ponds and the subsequent likelihood of hydrofracturing[10].

Most recent studies about AP surface melt focused on changes in melt extent and duration derived from remote sensing data[11-13], whereas the analysis of longer-term (decadal) changes in surface melt rate remained scarce[14-16]. Few studies have combined climate models and snowpack models to quantify long-term AP ice shelf melt rates[14,17], reporting a small but significant negative trend of AP surface melt rates between 1980 and 2021[17], possibly related to the AP warming hiatus post-1999[18]. Yet, in recent years, frequent and intense surface melt events have been observed in the AP with high melt rates[19-22]. In this context, it remains unclear whether the AP surface melt has undergone a statistically significant increase and what the associated drivers are.

Variations in AP surface melt rates arise from two primary factors: the changes in the occurrence frequency of surface melt and their intensity. Previous studies have highlighted the key role of changes in dynamic processes—specifically, changes in atmospheric circulation patterns—in driving the occurrence and variability of surface melt over the AP. For instance, melt episodes have been linked to Rossby wave trains originating from tropical forcing[23-27], as well as to the influence of atmospheric rivers and foehn winds that trigger surface melt and extreme warming events[20,21,27-29]. In addition to dynamic processes, thermodynamic processes—changes in the heat balance independent of atmospheric circulation—also play an important role in influencing the changes in surface melt rates and intensity. Key drivers include long-term near-surface warming driven by global climate change, variations in longwave radiation associated with the concentration of greenhouse gases and clouds, and changes in sea-ice extent and sea-surface temperatures (SST)[30-32]. For example, analyses of AP extreme warm events show no significant difference in atmospheric circulation before and after 1990[20,21]. Additionally, reductions in sea ice concentration in the Bellingshausen and Amundsen Seas from 1978 to 2020 have delayed the end of the melt season in West AP by enhancing turbulent heat fluxes[31]. This underscores the complex mechanisms driving changes in AP surface melt, as well as the potential importance of thermodynamics on surface melt variability.

In this work, to confirm the potential recent increase in AP surface melt rates, here we employ output from the advanced polar regional climate model (RCM), RACMO version 2.3p2[33], statistically downscaled from 27 km to a 2 km × 2 km grid[34]. RACMO2.3p2 faithfully represents AP surface melt volume/rate, compared with melt estimates from surface energy balance (SEB) model[35] in automatic weather stations ($R_{daily}^2 = 0.6$, $p < 0.01$; $RMSE_{daily} = 1.72$ mm w.e. day^{-1} between November and February). Firstly, in conjunction with another RCM (MAR v3.12), we quantify changes in AP surface melt rates. As a second step, we decompose total surface melt variability into two components: changes in melt frequency (related to dynamics) and melt intensity (related to thermodynamics), identified via a spatial clustering method, the self-organizing map (SOM). Finally, we further decompose the melt trends into the dynamic and thermodynamic contributions by holding frequency and intensity constant, respectively[30,36] (See Methods section). Our results demonstrate that AP surface melt rates have significantly increased during 2009–2022, primarily dictated by thermodynamics.

Results

Recent enhancement of the AP surface melt

From 1979 to 2022, AP surface melt occurred primarily between November and February (NDJF), averaging 73 Gt year^{-1} (161 mm w.e. year^{-1}, Supplementary Fig. 1b). NDJF accounts for 97% of the AP annual melt on average. Spatially, ice shelves dominate the AP surface melt (67%

of NDJF totals), with Wilkins, George VI, and northern Larsen ice shelves exhibiting the highest melt rates (Fig. 1a). Substantial surface melt (exceeding 100 mm w.e. yr^{-1} on average) also occurs along 25% of the grounded ice sheet margins.

Over the full NDJF period (1979-2022), surface melt rates show an overall but statistically insignificant negative trend (–0.2 Gt $year^{-2}$, Fig. 1b), while it exhibited a clear variability in different time-windows. Given the strong interannual variability, the 5-year low-pass Butterworth filtered time series highlights multi-year variability (red line in Fig. 1b) and long-term trends (Fig. 1c). AP experiences two periods with significantly negative trends in NDJF melt: 1992–2004 and 2003–2014 (Fig. 1c), when consistent significant negative trends were observed across all overlapping decadal windows. However, AP surface melt rates have shifted to a significant increase since 2009 (Fig. 1c), with a rate of 2.6 Gt $year^{-2}$ (5.7 mm w.e. $year^{-2}$, equivalent to 3% $year^{-1}$ relative to the 1981-2010 mean, $p<0.05$). This recent significant intensification is primarily concentrated over the western AP ice shelves and low-elevation grounded ice (Fig. 1d). The changes in AP surface melt align with near surface air temperature and surface energy budget anomalies, specifically net longwave radiation ($R^2=0.53$, $p<0.05$, Supplementary Fig. 2), which also shows significant increasing trends during 2009-2022 (0.3 W m^{-2} yr^{-1}, $p<0.05$). Independent simulations from another RCM, MAR v3.12 (Supplementary Fig. 3), corroborate these findings, confirming a pronounced and statistically significant enhancement in AP surface melt after 2009.

Circulation classification for AP surface melt

Next, we link surface melt to different atmospheric circulation patterns over the AP. After SOM clustering (see "Methods"), daily 500 hPa geopotential height anomaly maps from ERA5 reanalysis are classified into six patterns (Fig. 2). The six circulation patterns diverse high- and low-pressure configurations, reflecting the zonal variations of synoptic wave train and position of the Amundsen Sea low[28,37-39]. AP shows negative (positive) surface melt anomalies in SOM 1, 3 and 5 (SOM 2, 4 and 6), with corresponding surface energy budget anomalies (Supplementary Fig. 4 and 5). Specifically, when meridional winds are strong (SOM 2-5), consistent cloud cover anomalies across the entire AP modulate longwave radiation, which subsequently dominates surface melt (Supplementary Fig. 4-6). In contrast, when zonal winds prevail, the response is dipole-like: opposing cloud and radiation patterns in the western and eastern AP lead to melt anomalies dominated by longwave and shortwave radiation, respectively.

Here, we check the changes in circulation frequency and surface melt intensity (curve charts in Fig. 2), respectively. During 2009-2022—the period of significantly increasing melt—no significant trend is observed in the frequency of any individual circulation pattern. Instead, the average surface melt intensity shows a significant increase in five patterns, for instance 0.024 Gt d^{-1} $year^{-1}$ (0.05 mm w.e. d^{-1} $year^{-1}$) for SOM 6 ($p<0.05$, equivalent to 6% $year^{-1}$ relative to the 1981-2010 mean). This suggests that the recent enhancement in AP surface melt cannot be explained by shifts in atmospheric circulation frequency alone, highlighting the critical role of the intensification within-pattern which influences the surface melt intensity.

Thermodynamics as the dictating factor in recent melt enhancement

Surface melt trend decomposition (See Methods section) further demonstrates that thermodynamic processes—rather than large-scale circulation shifts—dominate, typically accounting for over 50% of the total trend across most periods characterized by significant AP surface melt trends (Supplementary Fig. 7). For the four typical periods with significant trends (Fig. 1c), while dynamics are responsible for 60% of the melt changes only during the 2003–2014 period, thermodynamics have dominated the post-2009 intensification, contributing 80% of the trend in RACMO2.3p2 and ~85% in MAR v3.12 (Supplementary Fig. 8a). Meanwhile, thermodynamic dominance is evident across the entire AP in RACMO2.3p2 and MARv3.12 (Fig. 3b and Supplementary Fig. 8d). This strong inter-model agreement underscores the robustness of the thermodynamic forcing in driving recent melt enhancement across the entire AP. Decomposition of individual SOM modes since 2009 further confirms this point (Fig. 3c). Thermodynamics have triggered significantly increasing trends in five patterns, such as SOM 2 (0.43 Gt $year^{-1}$/0.95 mm w.e. $year^{-1}$, $p<0.05$, 86% of total mode melt trend). Overall, these results indicate that thermodynamics dictate the recent acceleration of AP surface melt.

Surface energy budget anomalies for each circulation mode since 2009 identify the specific thermodynamic drivers (Fig. 3d). Downward longwave radiation increases significantly across four patterns, notably SOM 2 (0.8 W m^{-2} $year^{-1}$, p<0.05) and SOM 6 (0.9 W m^{-2} $year^{-1}$, p<0.05). Turbulent heat fluxes also exhibit upward trends, reaching statistical significance only in SOM 1 and SOM 2. In contrast, net shortwave radiation does not contribute to the surface energy balance increase, primarily due to a decline in downward shortwave (Supplementary Fig. 3b). These results suggest that thermodynamic intensification—modulating the increase in longwave radiation and turbulent heat flux over the AP— results in the recent enhancement of surface melt since 2009. This process is likely driven by atmospheric warming and cloud-radiative forcing, potentially amplified by positive feedback involving regional sea-ice loss and SST warming, which likely intensify turbulent heat fluxes (Supplementary Fig. 9). Together, our results demonstrate that thermodynamic-driven intensity changes, rather than circulation frequency, dictate the recent enhancement of NDJF surface melt on the AP.

Changes in extreme surface melt

Recent studies noted that more extreme climate events occurred over the Antarctic, impacting the Antarctic mass balance[21,27,40]. We estimate the changes in melt extremes over the AP (Fig. 4a) as the 90th percentile value of the 1979–2022 daily surface melt distribution in NDJF. Extreme surface melt accounts for an average of 23 Gt $year^{-1}$ (51 mm w.e. $year^{-1}$, 28% of total surface melt) in NDJF. Compared with non-extreme surface melt, these events are primarily characterized by large positive anomalies in melt (>200%) over the north AP (Supplementary Fig. 10). The total extreme surface melt rates declined rapidly after the early 1990s but shifted to a significant increase from 2013 onwards (Fig. 4a, b).

Trend decomposition analysis further demonstrates that recent changes in extreme melt since 2013 are predominantly thermodynamically driven (Fig. 4c). Throughout the entire record, 92% of the time windows exhibiting significant trends in extreme melt show a dominant thermodynamic contribution over dynamic factors. Specifically, for the post-2013 significant increase (2.7 Gt $year^{-2}$/5.9 mm w.e. $year^{-2}$), thermodynamics explain 86% of the observed trend. Historically, AP extreme melt events have been linked to transient synoptic processes and atmospheric circulation anomalies, like foehn winds or atmospheric rivers—extreme poleward water vapor transportation[21,27,41]. Our results, however, indicate that the recent changes in AP extreme surface melt events are rather dictated by thermodynamics. Consistent with previous reports of AP extreme warming[20,21], the amplification of AP heatwaves could be largely ascribed to long-term summer warming rather than atmospheric circulation trends.

Discussion

Since the satellite era, surface melt extent and volume over the Antarctic Peninsula have been reported to show a declining trend[13,17,42-44]. with most previous studies focusing on changes in melt extent and duration derived from satellite observations[13,42]. Consequently, the recent (since 2009) and statistically significant increase in AP surface melt rates and the reasons have not been previously reported. Using two independent polar RCMs, we demonstrate a clear reversal in AP surface melt trends since 2009, characterized by a significant NDJF increase of 3% year^{-1} (p<0.05) in RACMO2.3p2. Compared with the results of satellite observation, passive microwave data show that melt days remains consistent with our modeled melt rates (R^2=0.62, p<0.05; Supplementary Fig. 11), with an increasing trend of 0.02 d yr^{-1} since 2009 (p<0.05). However, melt extent trends tend to underestimate the recent intensification. This discrepancy suggests that the severity of AP melting may be underestimated using satellite observations alone. Our result of quantifying melt rates is an effective supplement to the signals captured by satellite observation.

Our analysis shows that this recent enhancement is primarily thermodynamically driven, rather than associated with changes in large-scale circulation. Our findings indicate that the thermodynamic signals are related to the recent increase in longwave radiation and turbulent heat flux. In addition, we also note that there is a surface melt peak in the early 1990s, similar highly positive longwave radiation and turbulent heat flux are also found along with early-peak of cloud cover anomalies. The dominant thermodynamic contribution likely reflects a combination of processes—largely independent of atmospheric circulation variability—including, for instance, regional atmospheric warming, water vapor and cloud cover increasing, nearby ocean warming and sea ice extent decline[30,32], which could impact the AP surface energy budget and melt intensity. These low-frequency thermodynamic forcings may increasingly govern Antarctic climate variability, as evidenced by the recent shift in sea-ice variability from high-frequency to low-frequency modes after 2007[45]. Consistent with this, ERA5 reanalysis indicates persistent SST warming in both the Weddell and Bellingshausen Seas during 2009-2022 NDJF (Supplementary Fig. 9), which likely enhanced turbulent heat fluxes, potentially influencing the surface melt over the AP[31].

The dominance of thermodynamic forcing does not imply that circulation variability is unimportant. Our decomposition associates daily melt with concurrent atmospheric circulation states, yet thermodynamic anomalies can also arise as a lagged response to prior circulation events. For the occurrence of strong surface melt over the AP, atmospheric circulation plays a critical role. Recent findings support that atmospheric rivers, föhn winds and teleconnections trigger AP surface melt and climate[20,27,46,47]. Circulations influence cloud cover anomalies and radiation budget as well as cause horizontal and vertical heat anomalies, consequently triggering melt anomalies. However, these dynamics cannot explain the recent increase and melt trends in AP surface melt from 2009 to 2022 fully. Specifically, for example, average NDJF 850 hPa horizontal heat advection and vertical motion do not show obvious enhancements over the AP since 2009 (Supplementary Fig. 12). However, thermodynamics like downward longwave radiation and turbulent flux contribute to the recent enhancement of surface melt through increasing melt intensity (Fig. 3 and Supplementary Fig. 2). Our results show the dynamics only dictate the significant decreasing trends during 2000s, when there is a decline in the occurrence frequency of circulation patterns related to negative surface melt anomalies (Fig. 2). Our discovery underscores the strong influence of thermodynamic drivers on surface melt across the AP, especially for the recent enhancement since 2009. A deeper investigation of these specific thermodynamic processes is essential for understanding AP surface melt and mass loss.

Methods

Modeled surface melt

We use daily surface melt rates of the polar (p) Regional Atmospheric Climate Model version 2.3p2 (RACMO2.3p2)[34] for the period 1979–2023. RACMO2.3p2 incorporates a 40-layer snow module that simulates surface melt, refreezing and retention in firn and subsequent runoff. The model is forced by ERA5 reanalysis data[48], which also prescribes the sea ice extent and sea surface temperature. The model ability to simulate surface mass balance (SMB) changes and polar climate has been widely tested over the ice sheets of Greenland and Antarctica[33,49-51]. RACMO2.3p2 is run at 27 km spatial resolution, and further statistically downscaled to 2 km, yielding improved local melt patterns notably nearby the grounding line, which are underestimated in the original RACMO2.3p2 at 27 km[34]. A more detailed description of this regional climate model can be found in van Wessem et al.[33] and Noël et al.[34]. Overall, RACMO2.3p2 can present Antarctic near surface climatology and SEB conditions well[33,35,51].

RACMO2.3p2 has a robust representation of Antarctic Peninsula (AP) surface melt at annual scales[34]. To further assess the performance of simulating surface melt over the AP, we used daily surface melt flux from a SEB model from Jakobs et al.[35]. Four automatic weather stations (AWSs, stars in Supplementary Fig. 1a) in the AP were used to run the SEB model to output surface melt flux: AWS18 at the grounding line of Larsen C ice shelf; AWS14、AWS15 and AWS17 installed on the ice shelf, all of which have surface melt records. The number of stations used for evaluation is so small because very few stations in Antarctica measure the radiation balance and hence are suitable to close the SEB, a prerequisite to quantify melt rate[52]. We applied the evaluation method of van den Broeke[53] to assess RACMO2.3p2 by 10-day average surface melt values. Although differences remain, the comparison between RACMO and SEB results demonstrates the capacity of RACMO2.3p2 to capture AP daily and monthly surface melt patterns (Supplementary Fig. 1c and d).

We also use the other polar regional climate model, Modèle Atmosphérique Régional (MAR v3.12)[54] to estimate daily surface melt rates for the period 1980–2023 and confirm the results of surface melt trends and subsequent contribution decomposition in RACMO2.3p2. MAR v3.12 is run at 35 km spatial resolution and forced by ERA5 to produce surface melt outputs during 1980–2023. More detailed description of this regional climate model can be found in Gorodetskaya et al.[21] and Dethinne et al.[54]. The model effectively represents near-surface climatology and surface melt rates, while sometimes overestimates the melt duration and extreme values[54], compared to SEB outputs in Jakobs et al.[35].

Categorization of circulation patterns

The self-organizing maps[55,56] were used to classify atmospheric circulation patterns, which is a neural network method for unsupervised classification. SOM has been successfully utilized to identify circulation patterns in previous climatology research and has been thought to be more effective and objective compared with other classification methods like k-means[30,57-59]. The linear initialization was used in the SOM training process to make it easier to duplicate results and be more stable relative to random initialization[58]. Settings of the SOM approach used here are listed in Supplementary Tab. 1.

In a SOM, the number of nodes determines how many distinct patterns the input data can be represented by[55,56]. Based on iteratively adjusting the similarity between each node's reference vector and the input data, the final classification is obtained. The number of nodes therefore defines the number of final classes. If the number of nodes is too small, different patterns may be merged and the diversity of the data cannot be fully captured; if it is too large, the resulting map becomes excessively detailed, making the classification difficult to present and interpret[30,60]. In this study, the number of the neural node was set to 2×3, corresponding to six circulation patterns. The input data were daily 500 hPa geopotential height anomalies obtained by subtracting the average annual cycle from ERA5 during 1979-2022 NDJF over the region 50°–85°W, 60°–75°S, and then multiplying the cosine of the latitude. We also tried other numbers of neural nodes from 2×2 to 6×5 (not shown here). Smaller nodes overgeneralize the circulation patterns over the AP, while bigger nodes identify too many overly similar patterns (Supplementary Fig. 13 and 14). Therefore, the map size of 2×3 was sufficient to capture various highly generalized circulation patterns, but sufficiently few to facilitate convenient presentation and prevent over-similarity among patterns. We obtained consistent circulation clustering results using the atmospheric reanalysis MERRA-2 (Supplementary Fig. 15), highlighting that our approach is robust and not affected by the reanalysis forcing.

Quantitative thermodynamic and dynamic contributions

Cassano et al.[36] and Horton et al.[30] separated the factors contributing to the temporal change in a variable of interest into a component resulting from 1) the change in the occurrence frequency (days) of daily circulation patterns in a cluster, 2) a change in the cluster-mean physical variable, and 3) a combination of the two effects. To investigate the drivers of AP surface melt changes post-1979, we isolate the contribution of thermodynamic and dynamic (circulation-driven) factors. Here, we defined the total surface melt anomaly as the sum of the product of the frequency of each pattern $f_{n,t}$ and the corresponding temporal-average daily surface melt anomaly $\overline{M_{n,t}}$:

$$M_t = \sum_{n=1}^{N} \overline{M_{n,t}}\, f_{n,t} \tag{1}$$

where n is the cluster type of daily circulation maps, N is the number of patterns and t every year. To mitigate potential biases arising from the seasonal cycle, we utilized daily surface melt anomalies subtracting the climatological daily mean, instead of absolute values in the decomposition framework. The long-term trends and statistical significance of the surface melt anomalies are consistent with those of the raw surface melt (Fig. 1). We further decomposed $\overline{M_{n,t}}$ and $f_{n,t}$ into time mean ($\overline{M_n}$ and $\overline{f_n}$) and deviation ($M'_{n,t}$ and $f'_{n,t}$) from time mean components:

$$M_t = \sum_{n=1}^{N}\left(\overline{M_n} + M'_{n,t}\right)\left(\overline{f_n} + f'_{n,t}\right) \tag{2}$$

Then, we differentiated the above equation with respect to time:

$$\frac{\mathrm{d}M_t}{\mathrm{d}t} = \sum_{n=1}^{N}\left(\overline{f_n}\,\frac{\mathrm{d}M'_{n,t}}{\mathrm{d}t} + \overline{M_n}\,\frac{\mathrm{d}f'_{n,t}}{\mathrm{d}t} + \frac{\mathrm{d}\left(M'_{n,t}f'_{n,t}\right)}{\mathrm{d}t}\right) \tag{3}$$

where, the components on the right-hand side from left to right mean the thermodynamic, dynamic and interaction contributions. For the thermodynamic contributions, here it refers to the fact that the response of surface melt intensity to changes in the background field temperature and local SEB, independent of changes in atmospheric circulation patterns. For example, under a constant circulation frequency, these drivers include changes in cloud cover, longwave radiation, downward shortwave radiation, and turbulent heat flux due to background field warming and increased atmospheric water content caused by global warming; changes in net shortwave radiation due to changes in surface albedo, such as snow grain degradation or meltwater accumulation[61]; and changes in sensible heat flux and longwave radiation due to the reduction of surrounding sea ice and rising sea surface temperatures.

For the dynamic (circulation-driven) contributions, it means the surface melt is associated with all individual atmospheric circulation patterns and influenced by the occurrence frequency of the circulation patterns, with the assumption of constant surface melt intensity. The third component represents a combination of thermodynamic and dynamic factors, reflecting the changes in pattern occurrences that result in changes in daily surface melt and acting on changes in the thermodynamic component. Generally, the value of this interaction component is smaller than the other two components. Note that the dynamic factors in this study refer to the dynamic changes driven by atmospheric circulation rather than glacier dynamics. We obtained similar results using MERRA-2 as forcing (Supplementary Fig. 16).

Extreme surface melt

We defined the AP extreme surface melt based on the statistical distribution of daily surface melt amounts integrated over the whole AP using the threshold of extreme melt. The extreme threshold is defined as the 90th percentile value of the daily surface melt distribution of 1979–2023. The threshold of the 90th percentile is a common statistical method of extremes and has been applied in studies of extreme melt and surface mass balance[62,63]. We also further defined the intensity as average daily extreme melt anomalies, relative to the NDJF average daily melt spanning from 1979 to 2022. For the long-term changes in total extreme surface melt rates in NDJF, the contributions of thermodynamic and dynamic factors were also computed.

Cloud cover, radiation and temperature

Monthly mean sea surface temperatures and large-scale turbulent heat fluxes, daily total cloud cover data came from ERA5. We also use daily shortwave and longwave radiation, sensible and latent heat fluxes and 2 m air temperature over the AP from RACMO2.3p2 (27 km×27 km) forced by ERA5 in 1979-2022 NDJF[33].

Anomalies and analysis of time series

Daily surface melt anomaly corresponding to each SOM pattern was computed by subtracting the average daily melt during the NDJF period spanning from 1979 to 2022. For the temporal change in surface melt during our study period, we utilized the five-year low-pass filtering process to remove high-frequency signals based on a fourth-order Butterworth filter. All reanalysis and contribution computing were based on the filtered (low-pass) time series of surface melt. When computing the correlation coefficients, the time series has been detrended in advance. For linear trends, the Durbin-Watson test was used to examine the first-order autocorrelation of linear regression residuals. When the time series has significant auto-correlation, the trend was assessed using the Hamed-Rao modified Mann-Kendall test[64].

Data Availability

The data supporting the findings and figure generation in this study have been deposited in the Figshare database under accession code 10.6084/m9.figshare.31901062 [https://doi.org/10.6084/m9.figshare.31901062] (ref.[65]). The ERA5 reanalysis data used in this study are available in the Copernicus Climate Data Store (CDS) at [https://cds.climate.copernicus.eu/datasets]. The daily surface melt flux data from the surface energy balance used in this study are available in the PANGAEA database under accession code 10.1594/PANGAEA.910473 [https://doi.pangaea.de/10.1594/PANGAEA.910473] (ref.[35]). The RACMO2.3p2 (2 km) data used in this study are available at [https://doi.org/10.1038/s41467-023-

43584-6] (ref.[34]) or via the authors without conditions (contact: bnoel@uliege.be). The daily MARv3.12 model files used in this study are available at [http://ftp.climato.be/fettweis/MARv3.12/Antarctica/].

Code Availability

Self-organizing maps code is available at http://www.cis.hut.fi/projects/somtoolbox/. Climate Data Toolbox for MATLAB is used in this study and is available at https://chadagreene.com/ (ref.[66]). All codes supporting the findings and drawing figures in this study will be made available on Figshare (https://doi.org/10.6084/m9.figshare.31908304) (ref.[67]).

References

1 Banwell, A. F., Willis, I. C., Macdonald, G. J., Goodsell, B. & MacAyeal, D. R. Direct measurements of ice-shelf flexure caused by surface meltwater ponding and drainage. *Nat. Commun.* **10**, 730 (2019).

2 Bell, R. E., Banwell, A. F., Trusel, L. D. & Kingslake, J. Antarctic surface hydrology and impacts on ice-sheet mass balance. *Nat. Clim. Change* **8**, 1044-1052 (2018).

3 Lai, C.-Y. *et al.* Vulnerability of Antarctica's ice shelves to meltwater-driven fracture. *Nature* **584**, 574-578 (2020).

4 Massom, R. A. *et al.* Antarctic ice shelf disintegration triggered by sea ice loss and ocean swell. *Nature* **558**, 383-389 (2018).

5 Shepherd, A., Wingham, D., Payne, T. & Skvarca, P. Larsen ice shelf has progressively thinned. *Science* **302**, 856-859 (2003).

6 Alley, K., Scambos, T., Miller, J., Long, D. & MacFerrin, M. Quantifying vulnerability of Antarctic ice shelves to hydrofracture using microwave scattering properties. *Remote Sens. Environ.* **210**, 297-306 (2018).

7 Scambos, T. *et al.* Ice shelf disintegration by plate bending and hydro-fracture: Satellite observations and model results of the 2008 Wilkins ice shelf break-ups. *Earth Planet. Sci. Lett.* **280**, 51-60 (2009).

8 van den Broeke, M. Strong surface melting preceded collapse of Antarctic Peninsula ice shelf. *Geophys. Res. Lett.* **32** (2005).

9 Scambos, T. A., Hulbe, C., Fahnestock, M. & Bohlander, J. The link between climate warming and break-up of ice shelves in the Antarctic Peninsula. *J. Glaciol.* **46**, 516-530 (2000).

10 van Wessem, J. M., van den Broeke, M. R., Wouters, B. & Lhermitte, S. Variable temperature thresholds of melt pond formation on Antarctic ice shelves. *Nat. Clim. Change* **13**, 161-166 (2023).

11 Kuipers Munneke, P. *et al.* Intense winter surface melt on an Antarctic ice shelf. *Geophys. Res. Lett.* **45**, 7615-7623 (2018).

12 Zhang, Z. *et al.* Toward a real validation of passive microwave snowmelt detection algorithms over the Antarctic Ice sheet. *Int. J. Appl. Earth Obs. Geoinf.* **125**, 103600 (2023).

13 Zheng, L., Zhou, C., Liu, R. & Sun, Q. Antarctic snowmelt detected by diurnal variations of AMSR-E brightness temperature. *Remote Sens.* **10**, 1391 (2018).

14 Costi, J. *et al.* Estimating surface melt and runoff on the Antarctic Peninsula using ERA-Interim reanalysis data. *Antarct. Sci.* **30**, 379-393 (2018).

15 Trusel, L. D., Frey, K. E., Das, S. B., Munneke, P. K. & van den Broeke, M. R. Satellite-based estimates of Antarctic surface meltwater fluxes. *Geophys. Res. Lett.* **40**, 6148-6153 (2013).

16 Kuipers Munneke, P., Picard, G., van den Broeke, M., Lenaerts, J. & van Meijgaard, E. Insignificant change in Antarctic snowmelt volume since 1979. *Geophys. Res. Lett.* **39** (2012).

17 Banwell, A. F., Wever, N., Dunmire, D. & Picard, G. Quantifying Antarctic-wide ice-shelf surface melt volume using microwave and firn model data: 1980 to 2021. *Geophys. Res. Lett.* **50**, e2023GL102744 (2023).

18 Turner, J. *et al.* Absence of 21st century warming on Antarctic Peninsula consistent with natural variability. *Nature* **535**, 411-415 (2016).

19 Bevan, S., Luckman, A., Hendon, H. & Wang, G. The 2020 Larsen C Ice Shelf surface melt is a 40-year record high. *Cryosphere* **14**, 3551-3564 (2020).

20 González-Herrero, S., Barriopedro, D., Trigo, R. M., López-Bustins, J. A. & Oliva, M. Climate warming amplified the 2020 record-breaking heatwave in the Antarctic Peninsula. *Commun. Earth Environ.* **3**, 122 (2022).

21 Gorodetskaya, I. V. *et al.* Record-high Antarctic Peninsula temperatures and surface melt in February 2022: a compound event with an intense atmospheric river. *npj Clim. Atmos. Sci.* **6**, 202 (2023).

22 Larour, E., Rignot, E., Poinelli, M. & Scheuchl, B. Physical processes controlling the rifting of Larsen C Ice Shelf, Antarctica, prior to the calving of iceberg A68. *Proceedings of the National Academy of Sciences* **118**, e2105080118 (2021).

23 Fogt, R. L. & Marshall, G. J. The Southern Annular Mode: variability, trends, and climate impacts across the Southern Hemisphere. *Wiley Interdiscip. Rev. Clim. Change* **11**, e652 (2020).

24 Barrand, N. E. *et al.* Trends in Antarctic Peninsula surface melting conditions from observations and regional climate modeling. *J. Geophys. Res.: Earth Surf.* **118**, 315-330 (2013).

25 Tedesco, M. & Monaghan, A. J. An updated Antarctic melt record through 2009 and its linkages to high-latitude and tropical climate variability. *Geophys. Res. Lett.* **36** (2009).

26 Clem, K. R., Bozkurt, D., Kennett, D., King, J. C. & Turner, J. Central tropical Pacific convection drives extreme high temperatures and surface melt on the Larsen C Ice Shelf, Antarctic Peninsula. *Nat. Commun.* **13**, 3906 (2022).

27 Wille, J. D. *et al.* Intense atmospheric rivers can weaken ice shelf stability at the Antarctic Peninsula. *Commun. Earth Environ.* **3**, 90 (2022).

28 Gonzalez, S., Vasallo, F., Recio-Blitz, C., Guijarro, J. A. & Riesco, J. Atmospheric patterns over the Antarctic Peninsula. *J. Clim.* **31**, 3597-3608 (2018).

29 Wille, J. D. *et al.* West Antarctic surface melt triggered by atmospheric rivers. *Nat. Geosci.* **12**, 911-916 (2019).

30 Horton, D. E. *et al.* Contribution of changes in atmospheric circulation patterns to extreme temperature trends. *Nature* **522**, 465-469 (2015).

31 Liang, L. *et al.* Delayed Antarctic melt season reduces albedo feedback. *Natl. Sci. Rev.* **10**, nwad157 (2023).

32 Newton, B., Sayanda, D. & Bonsal, B. Thermodynamic and dynamic components of winter temperature changes in western Canada, 1950–2020. *J. Clim.* **37**, 719-734 (2024).

33 van Wessem, J. M. *et al.* Modelling the climate and surface mass balance of polar ice sheets using RACMO2–

Part 2: Antarctica (1979–2016). *Cryosphere* **12**, 1479-1498 (2018).
34 Noël, B. *et al.* Higher Antarctic ice sheet accumulation and surface melt rates revealed at 2 km resolution. *Nat. Commun.* **14**, 7949 (2023).
35 Jakobs, C. L. *et al.* A benchmark dataset of in situ Antarctic surface melt rates and energy balance. *J. Glaciol.* **66**, 291-302 (2020).
36 Cassano, J. J., Uotila, P., Lynch, A. H. & Cassano, E. N. Predicted changes in synoptic forcing of net precipitation in large Arctic river basins during the 21st century. *J. Geophys. Res.: Biogeosci.* **112** (2007).
37 Fogt, R. L., Wovrosh, A. J., Langen, R. A. & Simmonds, I. The characteristic variability and connection to the underlying synoptic activity of the Amundsen-Bellingshausen Seas Low. *J. Geophys. Res.: Atmos* **117** (2012).
38 Raphael, M. N. *et al.* The Amundsen Sea low: Variability, change, and impact on Antarctic climate. *Bull. Am. Meteorol. Soc.* **97**, 111-121 (2016).
39 Wang, S. *et al.* On the drivers of temperature extremes on the Antarctic Peninsula during austral summer. *Clim. Dyn.* **59**, 2275-2291 (2022).
40 Siegert, M. J. *et al.* Antarctic extreme events. *Front. Environ. Sci.* **11**, 1229283 (2023).
41 Datta, R. T. *et al.* The effect of foehn-induced surface melt on firn evolution over the northeast Antarctic Peninsula. *Geophys. Res. Lett.* **46**, 3822-3831 (2019).
42 Bevan, S. L. *et al.* Decline in surface melt duration on Larsen C Ice Shelf revealed by the advanced scatterometer (ASCAT). *Earth and Space Science* **5**, 578-591 (2018).
43 Johnson, A., Hock, R. & Fahnestock, M. Spatial variability and regional trends of Antarctic ice shelf surface melt duration over 1979–2020 derived from passive microwave data. *J. Glaciol.* **68**, 533-546 (2022).
44 Luis, A. J., Alam, M. & Jawak, S. D. Spatiotemporal change analysis for snowmelt over the Antarctic ice shelves using scatterometers. *Frontiers in Remote Sensing* **3**, 953733 (2022).
45 Chen, R., Yang, X.-Y. & Wang, D. A significant transition of Antarctic sea ice variability in response to the shoaling of the Circumpolar Deep Water. *Advances in Atmospheric Sciences*, 1-19 (2025).
46 Laffin, M. K., Zender, C. S., van Wessem, M. & Marinsek, S. The role of föhn winds in eastern Antarctic Peninsula rapid ice shelf collapse. *Cryosphere* **16**, 1369-1381 (2022).
47 Li, X. *et al.* Tropical teleconnection impacts on Antarctic climate changes. *Nat. Rev. Earth Environ.* **2**, 680-698 (2021).
48 Hersbach, H. *et al.* The ERA5 global reanalysis. *Q. J. R. Meteorolog. Soc.* **146**, 1999-2049 (2020).
49 Lenaerts, J. T. *et al.* Climate and surface mass balance of coastal West Antarctica resolved by regional climate modelling. *Ann. Glaciol.* **59**, 29-41 (2018).
50 Noël, B., van de Berg, W. J., Lhermitte, S. & van den Broeke, M. R. Rapid ablation zone expansion amplifies north Greenland mass loss. *Sci. Adv.* **5**, eaaw0123 (2019).
51 van Dalum, C. T., van de Berg, W. J. & van den Broeke, M. R. Sensitivity of Antarctic surface climate to a new spectral snow albedo and radiative transfer scheme in RACMO2. 3p3. *Cryosphere* **16**, 1071-1089 (2022).
52 van den Broeke, M. R. *et al.* Contrasting current and future surface melt rates on the ice sheets of Greenland and Antarctica: Lessons from in situ observations and climate models. *PLOS Clim.* **2**, e0000203 (2023).
53 van den Broeke, M., König-Langlo, G., Picard, G., Munneke, P. K. & Lenaerts, J. Surface energy balance, melt and sublimation at Neumayer Station, East Antarctica. *Antarct. Sci.* **22**, 87-96 (2010).
54 Dethinne, T. *et al.* Sensitivity of the MAR regional climate model snowpack to the parameterization of the

assimilation of satellite-derived wet-snow masks on the Antarctic Peninsula. *Cryosphere* **17**, 4267-4288 (2023).

55 Hewitson, B. C. & Crane, R. G. Self-organizing maps: applications to synoptic climatology. *Clim. Res.* **22**, 13-26 (2002).

56 Kohonen, T. The self-organizing map. *Proc. IEEE* **78**, 1464-1480 (1990).

57 Cassano, J. J., Cassano, E. N., Seefeldt, M. W., Gutowski Jr, W. J. & Glisan, J. M. Synoptic conditions during wintertime temperature extremes in Alaska. *J. Geophys. Res.: Atmos* **121**, 3241-3262 (2016).

58 Jiang, N., Luo, K., Beggs, P. J., Cheung, K. & Scorgie, Y. Insights into the implementation of synoptic weather-type classification using self-organizing maps: an Australian case study. *Int. J. Climatol.* **35** (2015).

59 Preece, J., Wachowicz, L., Mote, T., Tedesco, M. & Fettweis, X. Summer Greenland blocking diversity and its impact on the surface mass balance of the Greenland ice sheet. *J. Geophys. Res.: Atmos* **127**, e2021JD035489 (2022).

60 Loikith, P. C., Lintner, B. R. & Sweeney, A. Characterizing large-scale meteorological patterns and associated temperature and precipitation extremes over the northwestern United States using self-organizing maps. *J. Clim.* **30**, 2829-2847 (2017).

61 Ryan, J. C., Cooper, M. G., Cooley, S. W., Rennermalm, Å. K. & Smith, L. C. Meltwater ponding has an underestimated radiative effect on the surface of the Greenland Ice Sheet. *Nat. Commun.* **16**, 8274 (2025).

62 Bonsoms, J., Oliva, M., López-Moreno, J. I. & Fettweis, X. Rising extreme meltwater trends in Greenland ice sheet (1950–2022): surface energy balance and large-scale circulation changes. *J. Clim.* **37**, 4851-4866 (2024).

63 McLeod, J. T. & Mote, T. L. Linking interannual variability in extreme Greenland blocking episodes to the recent increase in summer melting across the Greenland ice sheet. *Int. J. Climatol.* **36** (2016).

64 Hamed, K. H. & Rao, A. R. A modified Mann-Kendall trend test for autocorrelated data. *Journal of hydrology* **204**, 182-196 (1998).

65 Zhang, Q. L. *et al.* The recent enhancement of the surface melt over the Antarctic Peninsula dictated by thermodynamics date sets. figshare https://doi.org/10.6084/m9.figshare.31901062 (2026).

66 Greene, C. A. *et al.* The climate data toolbox for MATLAB. *Geochemistry, Geophysics, Geosystems* **20**, 3774-3781 (2019).

67 Zhang, Q. L. *et al.* The recent enhancement of the surface melt over the Antarctic Peninsula dictated by thermodynamics code. figshare https://doi.org/10.6084/m9.figshare.31908304 (2026).

Acknowledgements

X.F. and C.K. acknowledge the Consortium des Équipements de Calcul Intensif (CÉCI) and the Tier-1 supercomputer (Lucia) infrastructure for providing the computational resources required for running the MAR model simulations.

Funding Statement

This study was supported financially by the National Natural Science Foundation of China (Grant No. 42525607), the Climate Change Special Project of the China Meteorological Administration (Grant No. QBZZ202507), the S&T Development Fund of CAMS for funding (Grant No.

2026KJ006), and the Basic Research Fund of the Chinese Academy of Meteorological Sciences (Grant Nos. 2024Z007, 2023Z025, 2023Z004 & 2023Z015). M.R.v.d.B. is supported by the Horizon Europe OCEAN:ICE project (Grant No. 101059388), the EMBRACER project financed by the Netherlands Organisation for Scientific Research (NWO, Summit grant SUMMIT.1.034), and the European Research Council Synergy Grant project FirnMelt (ERC Grant No. 101224055). The computational resources for running the MAR model were supported by the Fonds de la Recherche Scientifique de Belgique (F.R.S.-FNRS) under Grant No. 2.5020.11, and by the Walloon Region under Grant Agreement No. 1910247. B.N. is a Research Associate of the Fonds de la Recherche Scientifique de Belgique F.R.S.-FNRS.

Author Contributions Statement

Q.Z., S.W. and M.D. designed the study. Q.Z. performed the study and prepared the manuscript. B.N. and M.R.v.d.B. provided daily surface melt rates from RACMO2.3p2 at 2 km. C.K. conducted the MAR v3.12 simulations at 35 km, and X.F. provided modelled outputs. B.H., S.W., B.N., M.R.v.d.B., X.F., C.K., D.Q. and M.D. contributed to discussing and commenting the results and editing the manuscript.

Competing Interests Statement

The authors declare no competing interests.

Figure Legends/Captions

Fig. 1 Changes in AP NDJF surface melt. **a** Spatial distribution of multi-year average surface melt from 1979-2022 November to February of the following year (NDJF). **b** Long-term NDJF surface melt change from 1979 to 2022. The solid red line represents the results after the five-year low-pass Butterworth filtering. The values in parentheses below the left y-axis tick labels represent the spatially averaged melt rates (mm w. e. yr^{-1}). The changes are also shown as a percentage (right y-axis, relative to the 1981–2010 mean). **c** Trends of AP surface melt in NDJF during different periods. Linear trends were computed based on the time series of NDJF surface melt after the five-year low-pass filtering. The start and end time-points of a tendency are defined as the period during which all overlapping 10-year windows exhibit a consistent, significant trend. **d** Spatial distribution of NDJF linear trends post-2009. The bold black line in (**a, d**) represents the extent of the AP. The grey dots in (**c, d**) represent passing the (Hamed-Rao modified) Mann-Kendall significance test of the confidence level of 95%.

Fig. 2 Circulation patterns and corresponding daily surface melt anomaly. **a-f** Spatial maps and accompanying time series for each of the six identified circulation patterns: SOM 1 (**a**), SOM 2 (**b**), SOM 3 (**c**), SOM 4 (**d**), SOM 5 (**e**), and SOM 6 (**f**). In the spatial maps, shading represents daily surface melt anomalies (%) relative to the average daily melt during the NDJF period spanning from 1979 to 2022. Contours (gpm) denote 500 hPa geopotential height anomalies (positive in red and negative in blue), and vectors 500 hPa wind field anomalies. The black numbers (%) express the circulation patterns fractions explained by each SOM. In the curve graphs, low-pass filtered lines illustrate the frequency of occurrence for each SOM pattern, along with the corresponding average AP-integrated melt rate anomalies (Gt d^{-1}). The values in parentheses below the right y-axis tick labels represent the spatially averaged melt rates (mm w. e. d^{-1}). The red numbers in the upper left corner of each curve graph denote the average surface melt anomaly and the fraction of melt produced for each pattern relative to the total NDJF melt. The black numbers (% yr^{-1}) and red numbers (Gt d^{-1} yr^{-1}) in the upper right corner of each curve graph denote the linear trends in frequency and average surface melt anomalies during 2009-2022 respectively. Bold numbers represent passing the (Hamed-Rao modified) Mann-Kendall significance test of the confidence level of 95%.

Fig. 3 Contribution of thermodynamic, dynamic and interaction processes to the surface melt trend. a Contributions of individual components to the surface melt trends during four typical periods. **b** Spatial thermodynamic contributions during 2009-2022. **c** Melt trends due to thermodynamics, dynamics and the interaction in each SOM node. **d** Trends in mean anomalies of net shortwave radiation (SW_{net}), downward longwave radiation (LWD) and turbulent heat flux (THF) in each mode during 2009-2022 NDJF. The values in parentheses below the y-axis tick labels in (**c**) represent the spatially averaged melt rates (mm w. e. yr^{-1}). The stars in (**c, d**) represent passing the (Hamed-Rao modified) Mann-Kendall significance test of the confidence level of 95%.

Fig. 4 Changes in extremes and contributions of the thermodynamics and dynamics. a Long-term change in total extreme surface melt in NDJF and intensity of extremes. The intensity represents average daily extreme melt anomalies, relative to average daily melt during the NDJF period spanning from 1979 to 2022. The solid lines represent the results after the five-year low-pass filtering. **b** Trends of extreme surface melt in NDJF during different periods. **c** Contribution (%) of thermodynamic, dynamic and the interaction factors to trends of total extreme surface melt rates. The values in parentheses below the y-axis tick labels in (**a**) represent the spatially averaged melt rates (mm w. e.).

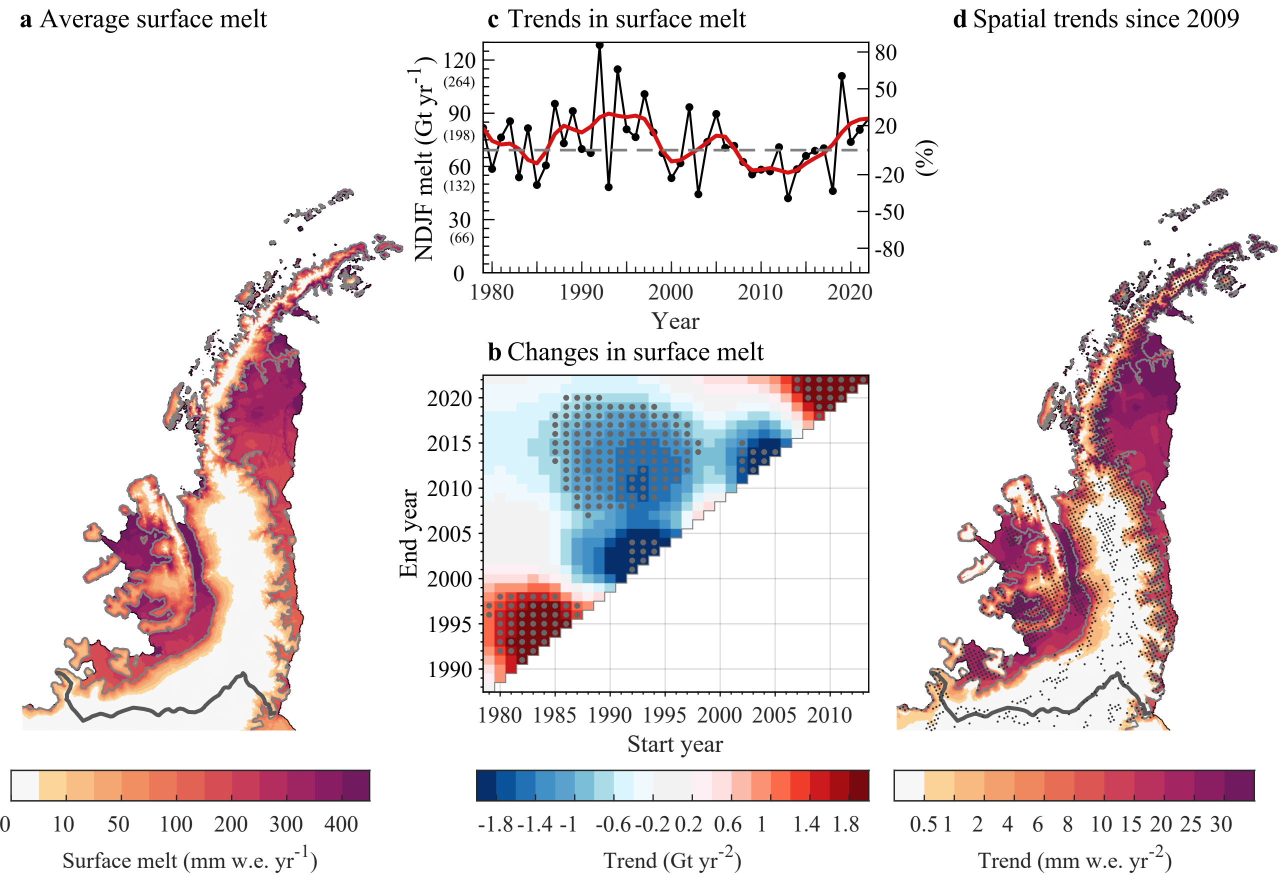

a Average surface melt
c Trends in surface melt
d Spatial trends since 2009
NDJF melt (Gt yr-1)
120 (264)
90 (198)
60 (132)
30 (66)
0
80
50
20
-20
-50
-80
(%)
1980
1990
2000
2010
2020
Year
b Changes in surface melt
End year
2020
2015
2010
2005
2000
1995
1990
1980
1985
1990
1995
2000
2005
2010
Start year
0
10
50
100
200
300
400
Surface melt (mm w.e. yr-1)
-1.8
-1.4
-1
-0.6
-0.2
0.2
0.6
1
1.4
1.8
Trend (Gt yr-2)
0.5
1
2
4
6
8
10
15
20
25
30
Trend (mm w.e. yr-2)

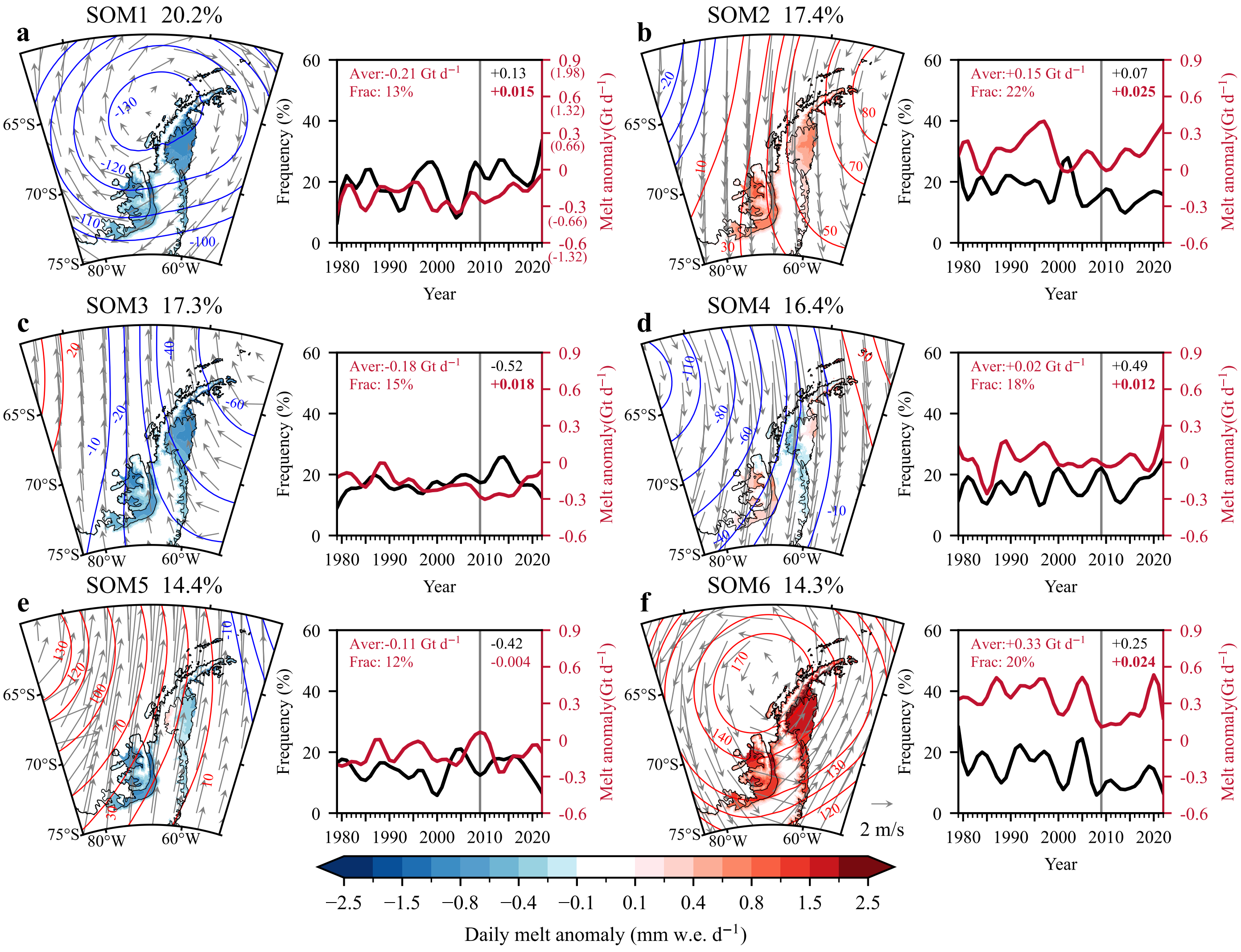

a
SOM1 20.2%
Aver:-0.21 Gt d^{-1}
Frac: 13%
+0.13
+0.015
b
SOM2 17.4%
Aver:+0.15 Gt d^{-1}
Frac: 22%
+0.07
+0.025
c
SOM3 17.3%
Aver:-0.18 Gt d^{-1}
Frac: 15%
-0.52
+0.018
d
SOM4 16.4%
Aver:+0.02 Gt d^{-1}
Frac: 18%
+0.49
+0.012
e
SOM5 14.4%
Aver:-0.11 Gt d^{-1}
Frac: 12%
-0.42
-0.004
f
SOM6 14.3%
Aver:+0.33 Gt d^{-1}
Frac: 20%
+0.25
+0.024
65°S
70°S
75°S
80°W
60°W
Frequency (%)
Melt anomaly(Gt d^{-1})
Year
(1.98)
(1.32)
(0.66)
(-0.66)
(-1.32)
2 m/s
−2.5
−1.5
−0.8
−0.4
−0.1
0.1
0.4
0.8
1.5
2.5
Daily melt anomaly (mm w.e. d^{-1})

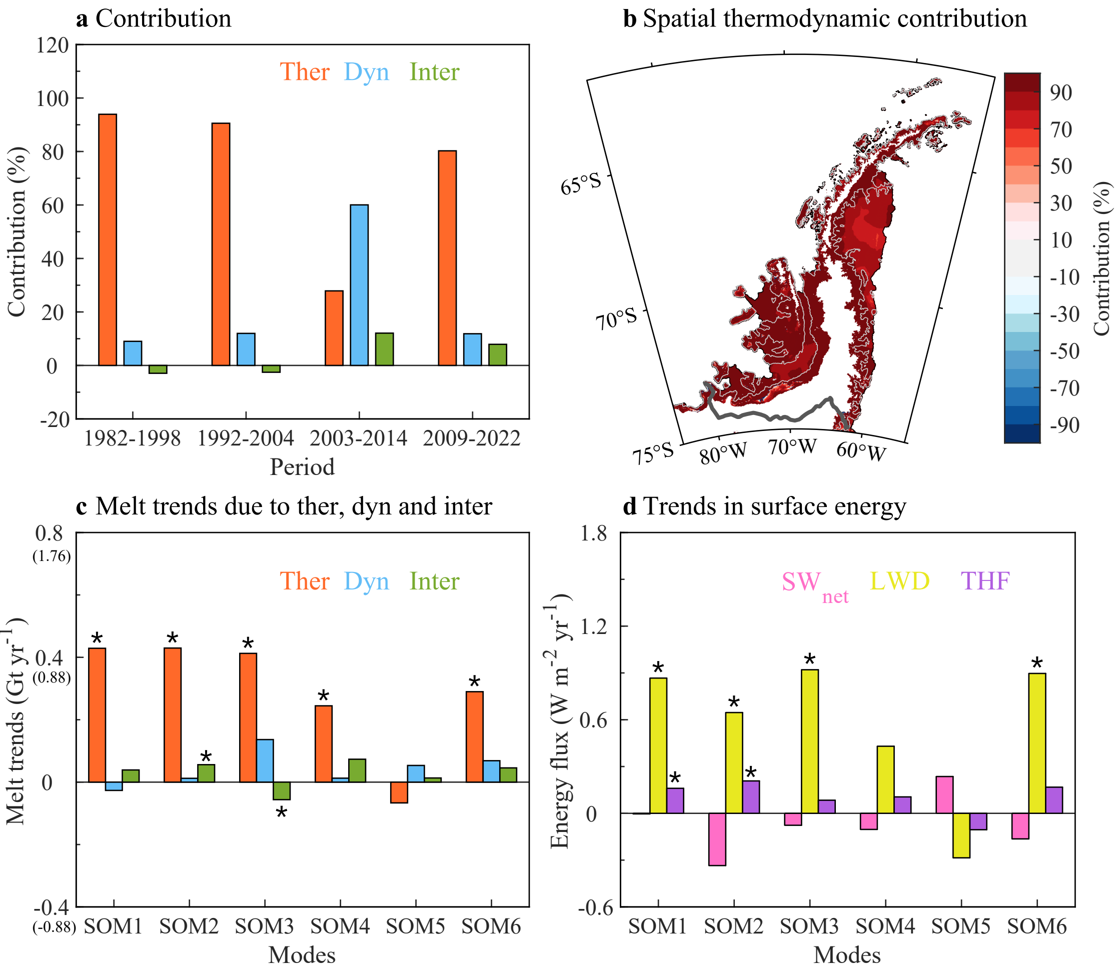

a Contribution
Ther Dyn Inter
Contribution (%)
120
100
80
60
40
20
0
-20
1982-1998
1992-2004
2003-2014
2009-2022
Period
b Spatial thermodynamic contribution
65°S
70°S
75°S
80°W
70°W
60°W
90
70
50
30
10
-10
-30
-50
-70
-90
Contribution (%)
c Melt trends due to ther, dyn and inter
Ther Dyn Inter
Melt trends (Gt yr^{-1})
0.8
(1.76)
0.4
(0.88)
0
-0.4
(-0.88)
SOM1
SOM2
SOM3
SOM4
SOM5
SOM6
Modes
d Trends in surface energy
SW$_{net}$ LWD THF
Energy flux (W m^{-2} yr^{-1})
1.8
1.2
0.6
0
-0.6
SOM1
SOM2
SOM3
SOM4
SOM5
SOM6
Modes

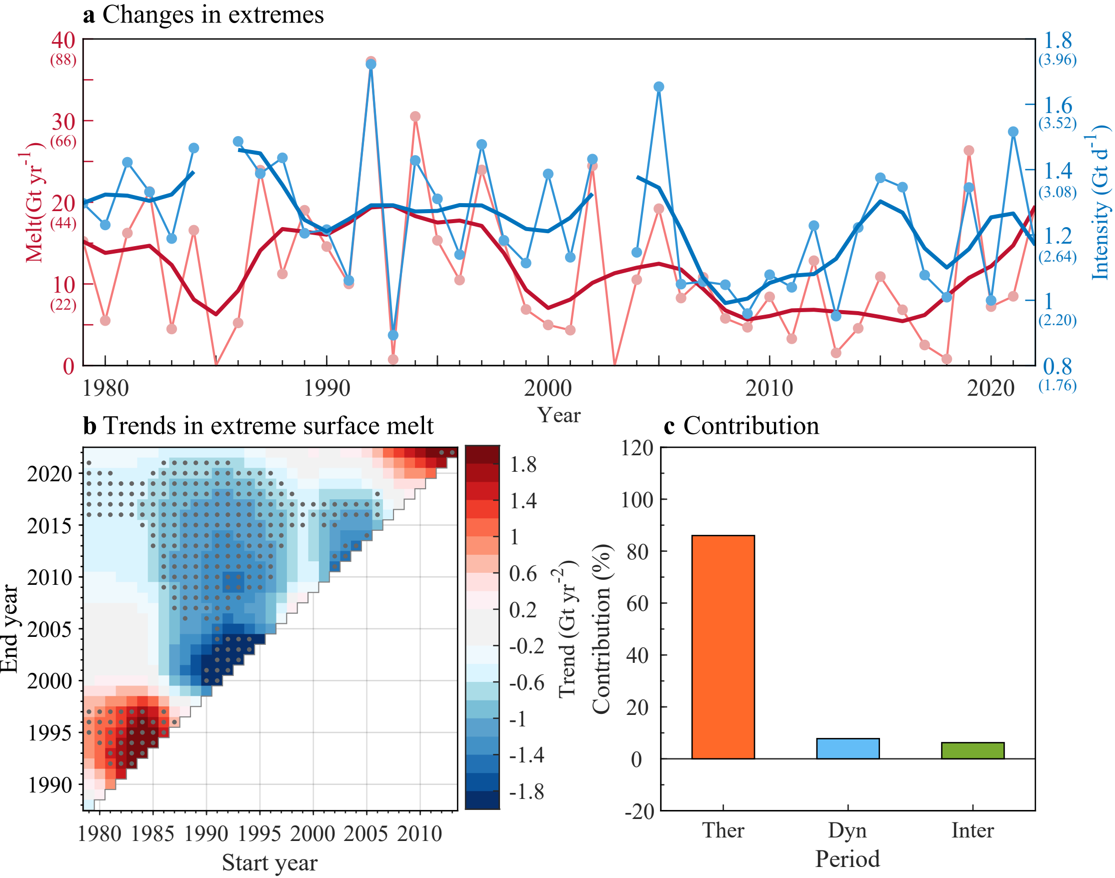
a Changes in extremes
Melt(Gt yr^-1)
40 (88)
30 (66)
20 (44)
10 (22)
0
Intensity (Gt d^-1)
1.8 (3.96)
1.6 (3.52)
1.4 (3.08)
1.2 (2.64)
1 (2.20)
0.8 (1.76)
1980
1990
2000
2010
2020
Year
b Trends in extreme surface melt
End year
2020
2015
2010
2005
2000
1995
1990
1980 1985 1990 1995 2000 2005 2010
Start year
Trend (Gt yr^-2)
1.8
1.4
1
0.6
0.2
-0.2
-0.6
-1
-1.4
-1.8
c Contribution
Contribution (%)
120
100
80
60
40
20
0
-20
Ther
Dyn
Inter
Period